Evaluation of optimal density weighting for regridding

Mark Bydder[a,*], Alexey A. Samsonov[b], Jiang Du[a]

[a]Department of Radiology, University of California San Diego, San Diego, CA 92103-8226, USA
[b]Department of Medical Physics, University of Wisconsin-Madison, Madison, WI 53792-1790, USA

Abstract

Density weighting is a necessary component of the regridding algorithm for interpolating nonuniformly sampled data points onto a regular grid. Differing concepts of optimality for the density weighting have been proposed previously. The present study reviews some of these concepts and evaluates the accuracy of different techniques by comparison with the image obtained by a computationally intensive least squares minimization. A variant on one of the techniques is proposed that yields the highest accuracy of those studied.
© 2007 Elsevier Inc. All rights reserved.

1. Introduction

Regridding is an important technique in magnetic resonance imaging (MRI) for interpolating nonuniformly sampled data points onto a rectilinear grid [1–6]. As described in previous studies [1–3], regridding provides an efficient means of approximating a solution to the inverse problem (Eq. (1))

$$\mathbf{Tm} = \mu \tag{1}$$

where $\mathbf{T}$ is an $m \times n$ matrix of sinc interpolation coefficients, μ is an m-vector of k-space points sampled at arbitrary locations and $\mathbf{m}$ is an n-vector of k-space points on a grid. The least squares solution to Eq. (1) is rarely calculated directly due to the high computational demands, although iterative methods have been proposed [7,8]. Regridding may be considered a single iteration method that approximates the solution to Eq. (1) as

$$\hat{\mathbf{m}} = \mathbf{T}^*\mathbf{D}\mu \tag{2}$$

where * denotes Hermitian transpose, $\mathbf{D} = \mathrm{diag}(\mathbf{d})$ is an $m \times m$ diagonal matrix and $\mathbf{d}$ is an m-vector referred to as the "density" weighting. The choice for $\mathbf{d}$ is critical in achieving the highest accuracy of the approximation. Eliminating μ between Eqs. (1) and (2) shows the relationship between $\mathbf{m}$ and $\hat{\mathbf{m}}$ to be $\hat{\mathbf{m}} = \mathbf{T}^*\mathbf{DTm}$. Following Refs. [1,2], the density

weighting may be considered optimal when $\mathbf{T}^*\mathbf{D}$ best approximates the pseudoinverse of $\mathbf{T}$.

By minimizing the sum of squares of the difference between $\mathbf{T}^*\mathbf{D}$ and the pseudoinverse of $\mathbf{T}$ (i.e., minimizing the Frobenius norm) under the constraint that $\mathbf{D}$ must have diagonal structure, the solution proposed in Ref. [1] was

$$\mathbf{d} = diag\left(\Theta \begin{bmatrix} \mathbf{I}_k & 0 \\ 0 & 0 \end{bmatrix} \Theta^* \right) \tag{3}$$

where $\mathbf{T} = \Theta \sum \Omega^*$ is the singular value decomposition (SVD) of $\mathbf{T}$ and $\mathbf{I}_k$ is the $k \times k$ identity matrix.

1.1. Kaiser–Bessel kernel

The dimensions of $\mathbf{T}$ for a typical MRI data set are m, n of the order 10^4–10^5; therefore, the computational requirements for calculations involving $\mathbf{T}$ are impractical for all but the smallest data sets. It is well known that the operation of $\mathbf{T}$ upon a vector can be approximated using interpolation kernels much narrower than sinc that reduce the number of nonzero terms to a tiny fraction of mn. For example, the Kaiser–Bessel kernel is able to achieve any required accuracy by optimizing the width and shape parameters [5,7]. The parameters chosen in the present study introduce a maximum error of 0.11% with only 16 nonzeros per row; thus, the Kaiser–Bessel interpolation matrix $\mathbf{H}$ is highly sparse.

The main consequence, other than a slight loss of accuracy, is that the result is convolved with the interpola-

tion kernel and so a deconvolution step is necessary. Letting be the $n \times n$ Fourier matrix and $\mathbf{U}$ be an $n \times n$ diagonal (deapodization) matrix, the deconvolution is represented by $\mathbf{QUQ}^*$. Thus, the action of $\mathbf{T}$ upon a vector is approximated as the deconvolution $\mathbf{QUQ}^*$ followed by multiplication with the $m \times n$ matrix $\mathbf{H}$ of Kaiser–Bessel interpolation coefficients. Then, Eqs. (1) and (2) become

$$\mathbf{HQUQ}^*\mathbf{m} = \mu \qquad (4)$$

$$\hat{\mathbf{m}} = \mathbf{QU}^*\mathbf{Q}^*\mathbf{H}^*\mathbf{D}\mu \qquad (5)$$

Letting $\mathbf{H} = \Theta \sum \Omega^*$ be the SVD of $\mathbf{H}$, the density is given by

$$\mathbf{d} = diag\left(\Theta \begin{bmatrix} \mathbf{I}_k & 0 \\ 0 & 0 \end{bmatrix} \Theta^* \right) \qquad (6)$$

Note that the matrix in square brackets in Eq. (6) is the result of $\sum^{-1}\sum$ and as such should have nonzero entries only where the singular values of $\sum$ are greater than a specified threshold. If no threshold is specified, then the expression is simply the identity matrix and $\mathbf{d}$ becomes a vector of 1's. Thus, other than for uniformly sampled data, a singular value threshold or some equivalent form of regularization is necessary to obtain a meaningful result.

2. Practical density methods

Despite its sparseness, $\mathbf{H}$ is still inconvenient for performing SVD since the resulting matrices are not sparse. Nevertheless, Eq. (6) can be computed on small data sets to enable comparison with other methods of calculating the density. Many such methods have been proposed; these tend to be motivated by geometrical considerations or different optimality criteria from those outlined above. As a starting point, let $\mathbf{e}_m$ be an m-vector of 1's, then the vector $\mathbf{H}^*\mathbf{e}_m$ gives an estimate of the sampling density on the grid points. The vector $\mathbf{HH}^*\mathbf{e}_m$ interpolates this estimate onto the sampled points and gives an estimate of the sampling density on the sampled points. Thus, the reciprocal of this vector can provide a reasonable estimate of the density weighting required to correct for nonuniform sampling [5].

$$\mathbf{d}_0 = 1/\mathbf{HH}^*\mathbf{e}_m \qquad (7)$$

As noted in Ref. [8], $\mathbf{d}_0$ is blurred by the interpolation kernel, which makes it unsuitable when the density has significant variation over the kernel width. An iterative scheme was proposed in Ref. [9] to improve upon the initial estimate $\mathbf{d}_0$; starting with $\mathbf{d} = \mathbf{d}_0$, successively accurate estimates are obtained from

$$\mathbf{d} = \mathbf{d}/\mathbf{HH}^*\mathbf{d} \qquad (8)$$

The rationale behind this approach is that the density weighting becomes optimal as $\mathbf{HH}^*\mathbf{d}$ approaches unity. Convergence can be slow and the solution does not apparently minimize a specific objective function. As shown

in Ref. [10], a better approach may be to pose the optimality condition as an inverse problem

$$\mathbf{HH}^*\mathbf{d} = \mathbf{e}_m \qquad (9)$$

and use standard techniques, such as iterative steepest descent, to find a solution. The convergence of this algorithm is well understood and the solution minimizes the least squared error objective function $\|\mathbf{HH}^*\mathbf{d} - \mathbf{e}_m\|_2$.

2.1. Nonnegativity and smoothness

Since the elements of $\mathbf{H}$ are all positive, it is implicit in Eqs. (7) and (8) that the density only contains positive values. Likewise, the matrix in square brackets in Eq. (6) can be written as $\Theta_k\Theta_k^*$, where $\Theta_k = \Theta\begin{bmatrix} \mathbf{I}_k & 0 \\ 0 & 0 \end{bmatrix}$, so the diagonal elements are equal to the sum of squares of the columns of Θ_k and cannot be negative.

By contrast, the least squares solution of Eq. (9) offers no guarantee of nonnegativity unless a specific constraint is introduced [11]. Similar equations posed in Refs. [1,2], based on solving $\mathbf{T}^*\mathbf{DT} = \mathbf{I}_n$, also place no restriction on the sign of the density weighting. The occurrence of negative values in $\mathbf{d}$ is difficult to interpret as a meaningful density or as an artifact of numerical instability, since it is usually the case that the interpolation matrix is ill conditioned. As shown in Results, applying regularization to Eq. (9) eliminates negative values from the result, which suggests they arise from numerical instability. Moreover, the unregularized solution (containing negative values) does not yield the highest accuracy for the regridded image. Thus, it is presumed in this study that the density weighting should be positive.

The matrix $\mathbf{D}$ may also be used to precondition the iterative solution of Eq. (1), particularly in relation to parallel imaging reconstruction [6]. Rather than solving Eq. (1) itself, the weighted normal equations are formed and the equation to be solved becomes $\mathbf{T}^*\mathbf{DTm} = \mathbf{T}^*\mathbf{D}\mu$. The weighting matrix in this case ($\mathbf{T}^*\mathbf{D}$) is an approximation of the pseudoinverse of $\mathbf{T}$, which is the ideal choice of preconditioner [12]. Weighting the data in this manner does perturb the solution from the true least squares minimum; however, the difference is negligible when the density is a smoothly varying function because nearby data points are weighted similarly. For this reason, it is also presumed in this study that the density weighting should be smoothly varying.

The purpose of introducing nonnegativity and smoothness assumptions in the density weighting is to provide a basis for the regularization of Eq. (9), which is necessary to overcome ill conditioning. As indicated by Eq. (6) and the singular value spectrum of the interpolation matrix (see Results), regularization is necessary to obtain a meaningful result whether by use of a singular value threshold (Eq. (6)), nonnegativity constraint (Eq. (8)) or one of many other regularization strategies [13].

2.2. Proposed method

The present study proposes using the preconditioned conjugate gradient (CG) algorithm to solve Eq. (9) combined
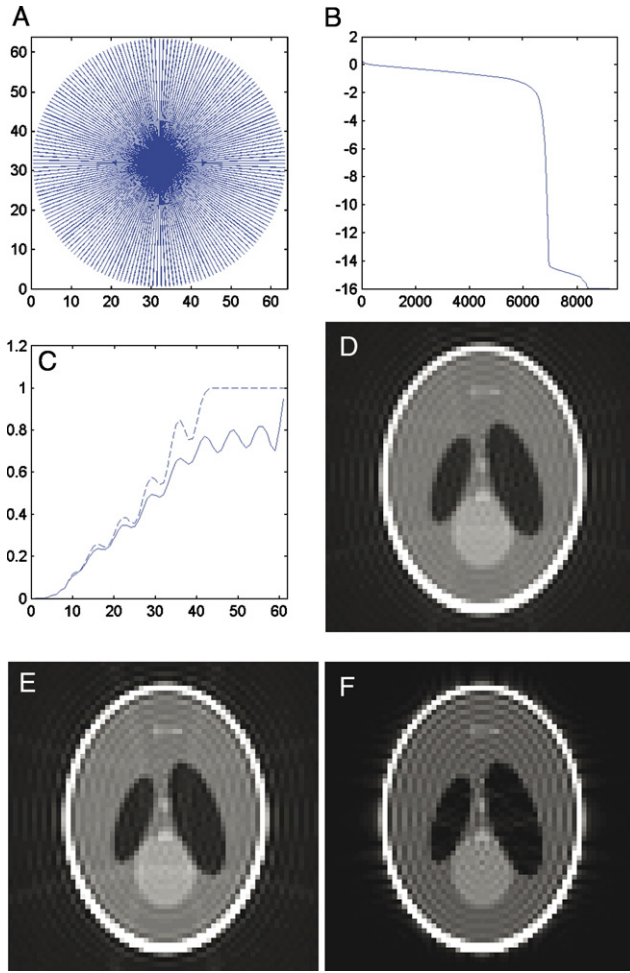
Fig. 1. (A) shows a plot of the trajectory. (B) shows a log plot of singular values of **H** down to 10^{-16}. (C) shows a plot of the density along one radial spoke calculated using Eq. (6) with singular value thresholds of 10^{-1} (solid line) and 10^{-6} (dashed line). (D) and (E) show regridded images calculated with these densities and (F) shows the "gold" standard least squares image.

with a simple regularization strategy that ensures the solution is nonnegative and smooth. The result is a fast, stable method for computing **d**. The basic idea is to solve Eq. (9) under the constraint that should be close to an estimate of the density that is both nonnegative and smooth. The choice of $\mathbf{d}_0$ as the estimate is ideal since it has the required properties and can be calculated inexpensively. As well as regularization, the term $\mathbf{e}_m$ in Eq. (9) can be replaced with $\mathbf{He}_n$, where $\mathbf{e}_n$ is an n vector of 1's, due to the fact that interpolating a vector of 1's to arbitrary coordinates also results in a vector of 1's. This means Eq. (9) may be viewed as the normal form of Eq. (10), which expresses the intuitive notion that the regridded k-space should be uniformly weighted.

$$\mathbf{H}^*\mathbf{d} = \mathbf{e}_n \tag{10}$$

Incorporating the regularization term into Eq. (10) yields the overall equation

$$\begin{bmatrix} \mathbf{H}^* \\ \omega\mathbf{I}_m \end{bmatrix} \mathbf{d} = \begin{bmatrix} \mathbf{e}_n \\ \omega\mathbf{d}_0 \end{bmatrix} \tag{11}$$

Table 1
The RMS errors for different SVD thresholds and methods corresponding to Figs. 1 and 2

	10^0	10^{-1}	10^{-2}	10^{-6}	Jackson	Pipe	Rasche	Present
Fig. 1	0.622	0.291	0.290	0.290	0.577	0.110	0.053	0.049
Fig. 2	0.689	0.331	0.322	0.324	0.592	0.158	0.138	0.120

In both cases, the SVD-based method is less accurate than the practical method and the present method gives the best approximation to the gold standard image.

where a scalar ω is used to control the constraint. The least squares solution to Eq. (11) minimizes the objective function $||\mathbf{H}^*\mathbf{d} - \mathbf{e}_n||_2^2 + \omega^2||\mathbf{d} - \mathbf{d}_0||_2^2$, which shows that **d** is a compromise between satisfying Eq. (10) and staying close to the initial estimate $\mathbf{d}_0$.

3. Preconditioning

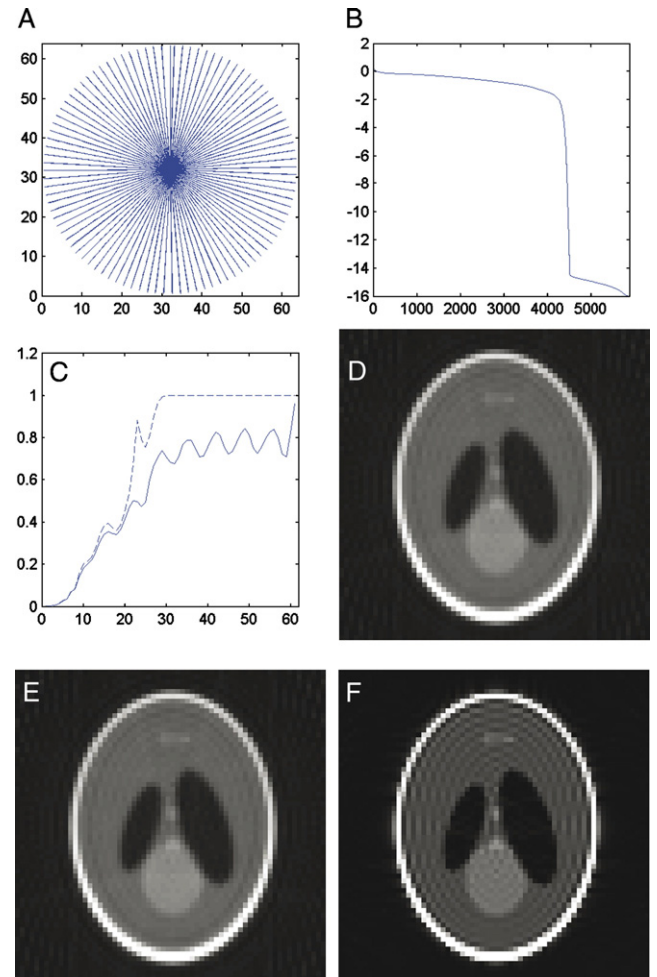Eq. (11) can be solved iteratively by CG on the normal equations [12], whereby Eq. (11) is transformed to

Fig. 2. (A) shows a plot of the trajectory. (B) shows a log plot of singular values of **H** down to 10^{-16}. (C) shows a plot of the density along one radial spoke calculated using Eq. (6) with singular value thresholds of 10^{-1} (solid line) and 10^{-6} (dashed line). (D) and (E) show regridded images calculated with these densities and (F) shows the "gold" standard least squares image.
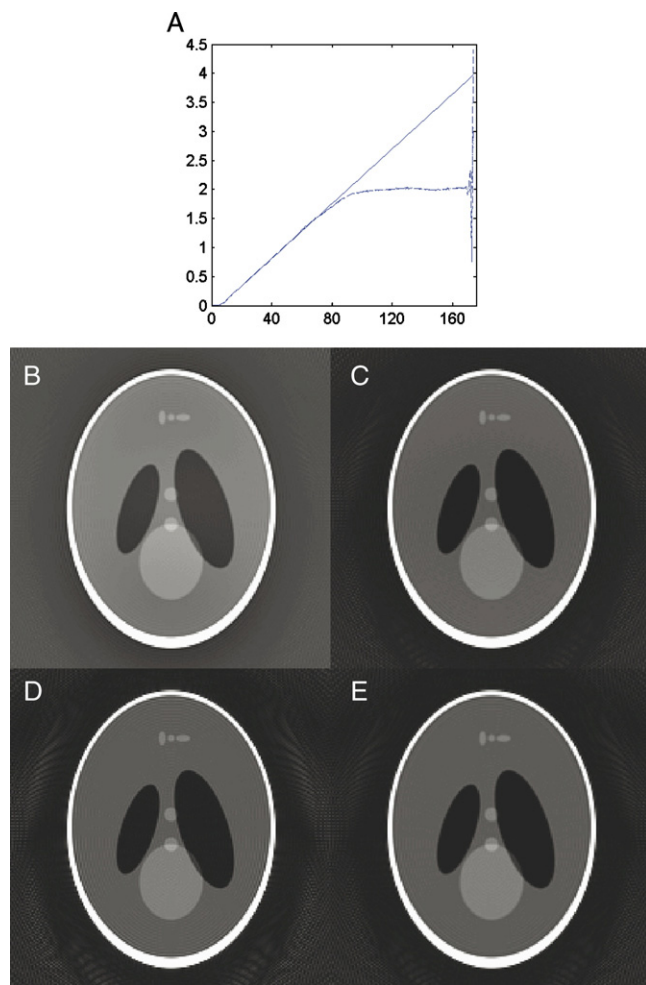
Fig. 3. (A) shows a plot of the density along one radial spoke for the full data set of Fig. 1: Jackson (dotted line), Pipe (dashed line), Rasche (solid line) and the present method (dash-dot line). (B)–(E) show regridded images using these densities.

Table 2
The RMS error for four different methods corresponding to (Figs. 3, 4 and 6)

	Jackson	Pipe	Rasche	Present
Fig. 3	0.565	0.111	0.122	0.074
Fig. 4	0.578	0.181	0.319	0.160
Fig. 6	0.575	0.071	0.067	0.041

As with Table 1, similar trends are observed between the different methods. The present method produces the most accurate images.

acquired on a 1.5 T TwinSpeed scanner (GE Healthcare, Wisconsin, USA) using a 5-in. surface coil. A radial ultrashort TE sequence was used [15,16]. The interpolation matrix was created using a Kaiser–Bessel kernel with width 4, oversampling factor 1.5 and shape parameter $2.05 \times$ width [7]. For small data sets, the SVD of $\mathbf{H}$ was calculated and the density was calculated by Eq. (6) using different values of threshold. Densities were also calculated from Eqs. (7), (8) and (11), and the Voronoi method [17]. The latter is a popular method that estimates the density from the area around each point on a Voronoi diagram.
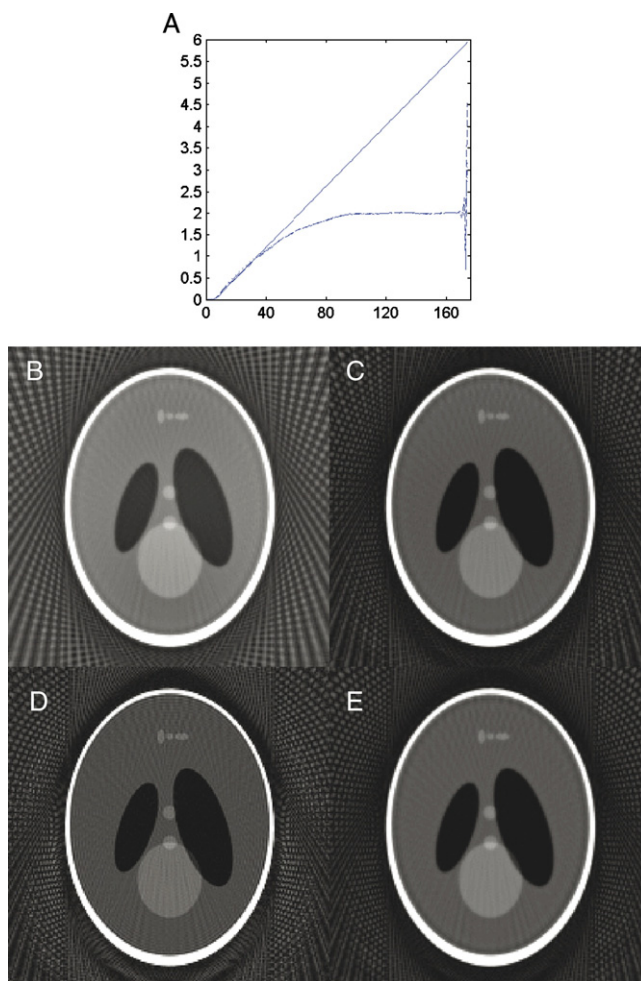
$(\mathbf{HH}^* + \omega^2 \mathbf{I}_m)\mathbf{d} = \mathbf{He}_n + \omega^2 \mathbf{d}_0$. It is advantageous to precondition the matrix equation to improve the rate of convergence. The optimal Jacobi preconditioner is the diagonal of $\mathbf{HH}^* + \omega^2 \mathbf{I}_m$ [12], which can be obtained by taking the 2-norms of the columns of $\mathbf{H}$. However, these calculations are computationally prohibitive. An alternative is to use the 1-norms, which are available inexpensively from the expression $\mathbf{g} = 1/\mathbf{d}_0 + \omega^2$, owing to the fact that $\mathbf{H}$ has positive elements only. The convergence with the 1-norms is inferior to the optimal choice but superior to the unpreconditioned case, particularly for small ω. The overall algorithm is given in Appendix A.

4. Materials and methods

Simulated data were created using the Shepp–Logan numerical phantom [14]. The Shepp–Logan phantom is a convenient choice since it resembles the structures and contrasts found in many clinical images, and the k-space data can be generated analytically. Actual MRI data were

Fig. 4. (A) shows a plot of the density along one radial spoke for the full data set of Fig 2. (B)–(E) show regridded images using these densities.

To define a "gold" standard image, the least squares solution of Eq. (4) was obtained by iterative CG until no changes in the image were observed (100 iterations, no preconditioning, no weighting). The normalized root-mean-square (RMS) difference between this image and the regridded image was used as a quantitative measure of the error. All computations were performed in MATLAB (The Mathworks, Massachusetts, USA) on a Xeon processor (Intel, California, USA). Unless otherwise stated, the default number of iterations was 10 and the value of ω was $2\times\max(\mathbf{H})$. The term "$\max(\mathbf{H})$" denotes the maximum element of $\mathbf{H}$ and was typically 0.3 to 0.5, since the rows of $\mathbf{H}$ are normalized by the area under the interpolation kernel.

5. Results

Initially, simulations were performed using small-sized data sets that permitted SVD of the interpolation matrix. For the less computationally demanding methods, comparisons were made using full-size simulated data sets representative of the typical matrix size, spatial resolution and number of acquired samples in an MRI acquisition; convergence and stability properties were assessed. Finally, actual MRI data were reconstructed.

Fig. 1 shows the results for a center-out radial trajectory comprising 191 spokes and 61 points per spoke regridded onto a 64×64 matrix. The interpolation matrix has dimensions $11,651\times9216$ and contains 184,899 nonzero elements. (A) shows a plot of the trajectory. (B) shows a log plot of singular values of $\mathbf{H}$ down to 10^{-16}. (C) shows a plot of the density along one radial spoke calculated using Eq. (6) with singular value thresholds of 10^{-1} (solid line) and 10^{-6} (dashed line). (D) and (E) show regridded images calculated with these densities and (F) shows the "gold" standard least squares image. Within the SVD threshold range shown, the images are similar although
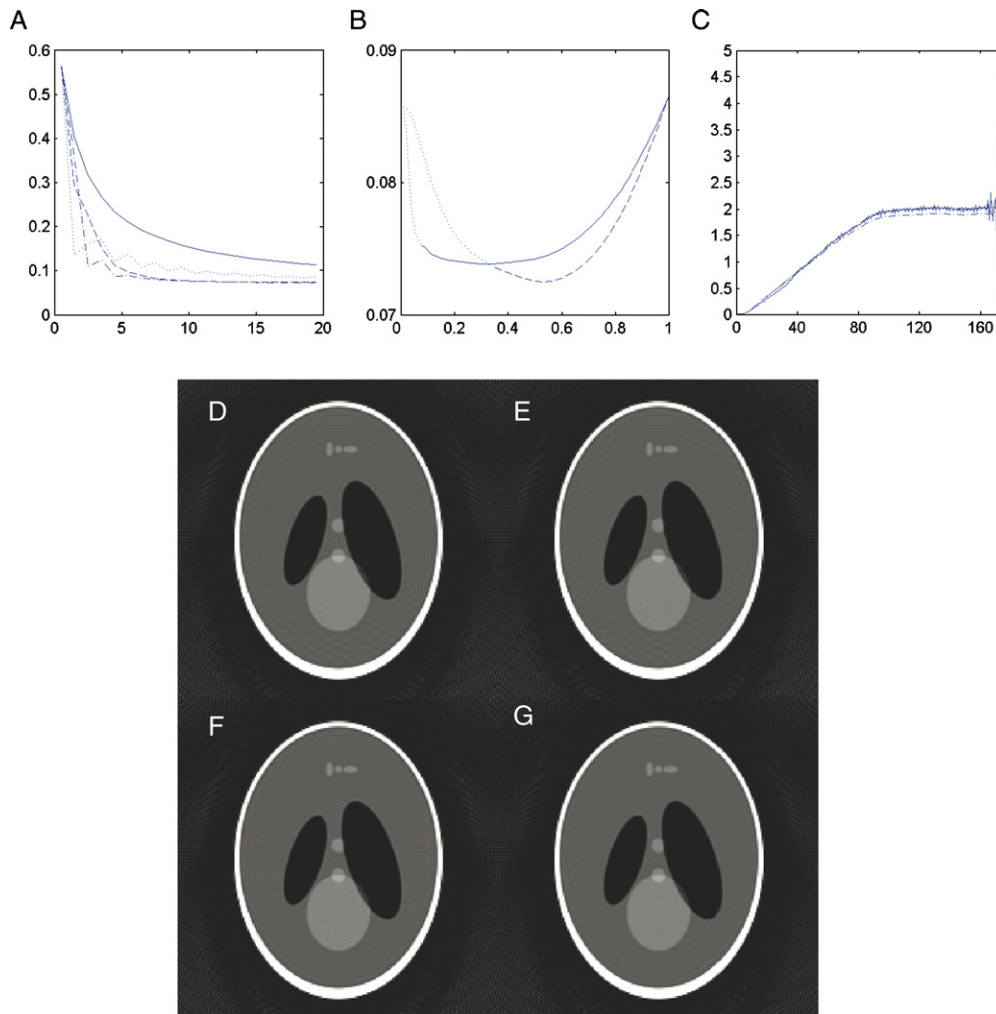

Fig. 5. (A) shows a plot of RMS error vs. iteration number for four methods: Pipe's (solid line), Eq. (11) using nonnegative steepest descent [11] and $\omega=0$ (dotted line), Eq. (11) with constraint $\mathbf{d_0}$ from Eq. (7) and $\omega=2\times\max(\mathbf{H})$ (dashed line) and Eq. (11) with constraint $\mathbf{d_0}=\mathbf{0}$ and $\omega=0.5\times\max(\mathbf{H})$ (dot-dashed line). (B) shows a plot of the RMS error vs. ω for the latter two methods after 20 iterations: $\mathbf{d_0}$ from Eq. (7) (solid line) and $\mathbf{d_0}=\mathbf{0}$ (dashed line). The scale of the x-axis is from 0 to $5\times\max(\mathbf{H})$ and 0 to $\max(\mathbf{H})$, respectively. The dotted line indicates the presence of negative values in the density. (C) shows a plot of the densities after 100 iterations. (D)–(G) show images for four methods after 100 iterations.

outside this range the images are severely degraded. The RMS errors for these images are in Table 1.

Fig. 2 shows the results for a similar trajectory to Fig. 1 but using only 96 spokes to give a 2× speedup as per a parallel acquisition [6]. The interpolation matrix $\mathbf{H}$ has dimensions 5856×9216 and contains 92,848 nonzero elements. (A) shows a plot of the trajectory. (B) shows a log plot of singular values of $\mathbf{H}$ down to 10^{-16}. (C) shows a plot of the density along one radial spoke calculated using Eq. (6) with singular value thresholds of 10^{-1} (solid line) and 10^{-6} (dashed line). (D) and (E) show regridded images calculated with these densities and (F) shows the "gold" standard image. The RMS errors are in Table 1.

Fig. 3 shows results using the full data set of Fig. 1 (174 point per spoke) from different density methods: Jackson (dotted line), Pipe (dashed line), Rasche (solid line) and the present method (dash-dot line). (A) shows a plot of the density along one radial spoke. (B)–(D) show regridded images using these densities. The RMS errors are in Table 2.

Fig. 4 shows results using the full data set of Fig. 2 (174 point per spoke) from different density methods: Jackson (dotted line), Pipe (dashed line), Rasche (solid line) and the present method (dash-dot line). (A) shows a plot of the density along one radial spoke. (B)–(D) show regridded images using these densities. The RMS errors are in Table 2.

Fig. 5 shows the results for the radial trajectory of Fig. 3. (A) shows a plot of RMS error vs. iteration number for four methods: Pipe's (solid line), Eq. (11) using nonnegative steepest descent [11] and $\omega=0$ (dotted line), Eq. (11) with constraint $\mathbf{d}_0$ from Eq. (7) and $\omega=2\times\text{max}(\mathbf{H})$ (dashed line) and Eq. (11) with constraint $\mathbf{d}_0=\mathbf{0}$ and $\omega=0.5\times\text{max}(\mathbf{H})$ (dot-dashed line). (B) shows a plot of the RMS error vs. ω for the latter two methods after 20 iterations: $\mathbf{d}_0$ from Eq. (7) (solid line) and $\mathbf{d}_0=\mathbf{0}$ (dashed line). The scale of the x-axis is from 0 to $5\times\text{max}(\mathbf{H})$ and 0 to $\text{max}(\mathbf{H})$, respectively. The dotted line indicates the presence of negative values in the density, which are considered unacceptable. Negative values evidently arise due to the poor numerical condition of $\mathbf{H}$ and can be avoided by increasing ω. (C) shows a plot of the densities after 100 iterations.

These plots show that Pipe's method converges relatively slowly and that the minimum RMS error does not necessarily correspond with $\omega\rightarrow0$; that is, regularization improves the accuracy of the density. (D)-(G) show images for four methods after 100 iterations: Pipe's method, nonnegative steepest descent, Eq. (11) with $\mathbf{d}_0$ from Eq. (7) and $\omega=2\times\text{max}(\mathbf{H})$ and Eq. (11) with $\mathbf{d}_0=\mathbf{0}$ and $\omega=0.5\times\text{max}(\mathbf{H})$. The RMS errors for these images are 0.082, 0.078, 0.074 and 0.072. The differences are minor, although Pipe's method and nonnegatively constrained least squares exhibit fast oscillation at high iteration counts and the resulting images contain similar (streak) artifacts (bottom center).
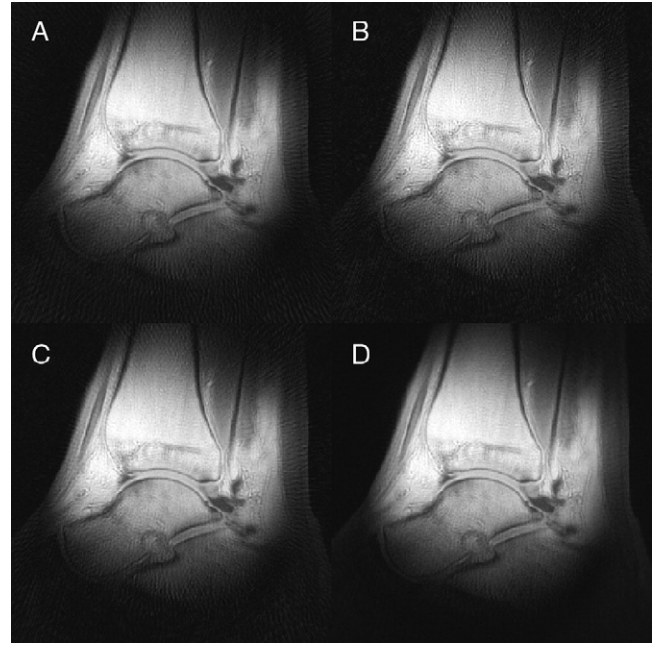

Fig. 6. (A)–(D) show images from Pipe, Rasche, the present method and least squares.

Fig. 6 shows the results from a center-out radial data set (255 spokes and 255 points per spoke regridded onto a 256×256 matrix). (A)-(D) show images from Pipe, Rasche, the present method and least squares. Visually, there is little difference between the images, although the RMS errors in Table 2 indicate greatest accuracy with the proposed method.

6. Discussion

The purpose of the present article has been to evaluate several methods for computing the density function. The two principal methods studied are those due to Sedarat and Nishimura [1] and Pipe and Menon [9], but the methods due to Jackson et al. [5] and Rasche et al. [17] are also considered; a variant of Pipe's method is proposed based on work by Samsonov et al. [10]. None of the approaches gives identical results, although the methods that derive from optimization of a specific objective function may be considered optimal in a specific sense.

As a comparison metric, the RMS difference between the regridded image and a "gold" standard reference image was used. The gold standard was calculated by a least squares minimization, which follows the idea of minimizing the difference between images produced by least squares and regridding $\|\mathbf{m}-\hat{\mathbf{m}}\|$ [1,2]. Various matrix approximations and weighting schemes were described in Ref. [1] using sinc and Kaiser–Bessel interpolation matrices ($\mathbf{T}$ and $\mathbf{H}$, respectively). In the present study, the Kaiser–Bessel scheme only was considered due to the high computational requirements for the sinc interpolation

matrix. Thus, the optimal density is given by Eq. (6); the result depends strongly on the choice of SVD threshold and cannot contain negative values.

The goal of Pipe's method is to find a vector $\mathbf{d}$ such that $\mathbf{HH}^*\mathbf{d}$ is unity, which corresponds to optimizing the point-spread function to be a delta function. By contrast with Sedarat and Nishimura's [1] method, it is computationally fast and requires no parameter choices, although it implicitly contains a nonnegativity constraint. Simulation studies in Figs. 1 and 2 and Table 1 indicate that Pipe's method produces superior images (in terms of the RMS error).

Comparison of Pipe's method with those of Jackson and Rasche shows that Pipe's method also generally produces superior images with computation times of the same order of magnitude. A variant of Pipe's scheme proposed in this study permits further improvement in accuracy. The goal of these methods is to find $\mathbf{d}$ such that $\mathbf{H}^*\mathbf{d}=\mathbf{e}_n$, which relies upon the notion that the regridded k-space should have uniform weighting. Whereas the present study uses conjugate gradient iteration, Pipe used a novel ratio technique to calculate the final solution. The ratio technique ensures a nonnegative result, but the convergence and stability properties of this method are uncertain. Results show slower convergence and introduced artifacts at high iteration counts. Conjugate gradient has faster convergence but requires explicit handling of the numerical ill conditioning by way of regularization (or a nonnegativity constraint).

The disadvantage is that an explicit regularization parameter must be introduced, although, in fairness, the underlying matrix is the same for both, so some form of regularization is necessary. A common regularization technique is 0th-order regularization [13], which may be considered a special case of the proposed method when the constraint vector is zero (i.e., $\mathbf{d}_0=\mathbf{0}$). With $\mathbf{d}_0=\mathbf{0}$ as the constraining vector, the density weighting is lower than the unconstrained solution wherever the data sampling is sparse. For radial sampling, this occurs at the edges of k-space and so the constraint suppresses high frequencies, which has the effect of low-pass filtering the image. It was found that the density weighting of Rasche tends to emphasize high frequencies, which has the effect of high-pass filtering. Noise in the final image reflects the nonuniform weighting of the frequencies, although this nonuniformity can be rectified by post-compensation, if required [8]. The nonuniform sampling also causes nonuniform noise variance in k-space will affect the image quality independently of the density weighting [18].

Appendix A

A preconditioned CG algorithm based on Ref. [12] for solving Eq. (11) is given in MATLAB. The input argument $\mathbf{H}$ is the interpolation matrix, ω is a scalar controlling the constraint and *iter* is the number of iterations. Suggested values are $w=2*\max(\max(\mathbf{H}))$ and iter$=10$. Note $\mathbf{d}_0$ (from Eq. (7)) is used as an initial estimate, as the constraint vector and as a component of the preconditioner.

```
function d=density(H,w,iter)
[m n]=size(H);
d=1./(H*(H'*ones(m,1)));
g=1./d+w^2;
r=H*(ones(n,1)-H'*d);
s=r./g;
new=r'*s;
for i=1:iter
    q=H*(H'*s)+w^2*s;
    alpha=new/(s'*q);
    d=d+alpha*s;
    r=r-alpha*q;
    q=r./g;
    old=new;
    new=r'*q;
    s=q+(new/old)*s;
end
```

References

[1] Sedarat H, Nishimura DG. On the optimality of the gridding reconstruction algorithm. IEEE Trans Med Imaging 2000;19:306.

[2] Rosenfeld D. An optimal and efficient new gridding algorithm using singular value decomposition. Magn Reson Med 1998;40:14.

[3] Van de Walle R, Barrett HH, Myers KJ, Altbach MI, Desplanques B, Gmitro AF, et al. Reconstruction of MR images from data acquired on a general nonregular grid by pseudoinverse calculation. IEEE Trans Med Imaging 2000;19:1160.

[4] O'Sullivan J. A fast sinc function gridding algorithm for Fourier inversion in computer tomography. IEEE Trans Med Imaging 1985; MI-4:200.

[5] Jackson JI, Meyer CH, Nishimura DG, Macovski A. Selection of a convolution function for Fourier inversion using gridding. IEEE Trans Med Imaging 1991;10:473.

[6] Pruessmann KP, Weiger M, Bornert P, Boesiger P. Advances in sensitivity encoding with arbitrary k-space trajectories. Magn Reson Med 2001;46:638.

[7] Matej S, Fessler JA, Kazantsev IG. Iterative tomographic image reconstruction using Fourier-based forward and back-projectors. IEEE Trans Med Imaging 2004;23:401–12.

[8] Pauly JM. Lecture notes in medical image reconstruction. http://www.stanford.edu/class/ee369c/notes/non_cart_recon.pdf.

[9] Pipe JG, Menon P. Sampling density compensation in MRI: rationale and an iterative numerical solution. Magn Reson Med 1991;41:179.

[10] Samsonov AA, Kholmovski EG, Johnson CR. Determination of the sampling density compensation function using a point spread function modeling approach and gridding approximation. Proc Intl Soc Magn Reson Med 2003;477.

[11] Kaufman L. Maximum likelihood, least squares, and penalized least squares for PET. IEEE Trans Med Imaging 1993;12:200.

[12] Shewchuk JR. Conjugate gradient without the agonizing pain. http://www.cs.cmu.edu/~quake-papers/painless-conjugate-gradient.pdf.

[13] Press WH, Teukolsky SA, Vetterling WT, Flannery BP. In: Cowles L, Harvey A, editors. Numerical recipes in C. 2nd ed. Cambridge: Cambridge University Press; 1992. p. 805.

[14] Ouwekerk R. (Johns Hopkins University Dept. Radiology). Source code for mriphantom.m.

[15] Robson MD, Gatehouse PD, Bydder M, Bydder GM. Magnetic resonance: an introduction to ultrashort echo-time imaging. J Comput Assist Tomogr 2003;27:825.

[16] Brittain JH, Shankaranarayanan A, Ramanan V, Shimakawa A, Cunningham CH, Hinks S, et al. Ultra-short TE imaging with single-digit (8 μs) TE. Proc Intl Soc Magn Reson Med 2004;629.

[17] Rasche V, Proksa R, Sinkus R, Bornert P, Eggers H. Resampling of data between arbitrary grids using convolution interpolation. IEEE Trans Med Imaging 1999;185:385.

[18] Newbould R, Liu C, Bammer R. Colored noise and effective resolution: data considerations for non-uniform k-space sampling reconstructions. Proc Intl Soc Magn Reson Med 2006;2939.